RSC Advances

PAPER

View Article Online
View Journal | View Issue

Check for updates

Cite this: *RSC Adv.*, 2018, **8**, 31121

Mesoporous anodic α-Fe_2O_3 interferometer for organic vapor sensing application

Feng-Xia Liang,[a] Lin Liang,[a] Xing-Yuan Zhao,[a] Xiao-Wei Tong,[b] Ji-Gang Hu,*[b] Yi Lin,[a] Lin-Bao Luo *[b] and Yu-Cheng Wu *[a]

In this work, we reported the utilization of mesoporous α-Fe_2O_3 films as optical sensors for detecting organic vapors. The mesoporous α-Fe_2O_3 thin films, which exhibited obvious Fabry–Perot interference fringes in the reflectance spectrum, were successfully fabricated through electrochemical anodization of Fe foils. Through monitoring the optical thickness of the interference fringes, three typical organic species with different vapor pressures and polarities (hexane, acetone and isopropanol) were applied as probes to evaluate the sensitivity of the α-Fe_2O_3 based interferometric sensor. The experiment results showed that the as-synthesized mesoporous α-Fe_2O_3 interferometer displayed high reversibility and stability for the three organic vapors, and were especially sensitive to isopropanol, with a detection limit of about 65 ppmv. Moreover, the photocatalytic properties of α-Fe_2O_3 under visible light are beneficial for degradation of dodecane vapor residues in the nano-pores and refreshment of the sensor, demonstrating good self-cleaning properties of the α-Fe_2O_3-based interferometric sensor.

Received 24th July 2018
Accepted 24th August 2018

DOI: 10.1039/c8ra06261g

rsc.li/rsc-advances

1. Introduction

Gas sensors have attracted considerable attention for their wide application in numerous areas such as air monitoring, gas (toxic, flammable and explosive) detection, medical diagnosis and food safety.[1] To date, much effort has been devoted to the design of small, low-cost and fast-response gas sensors with high sensitivity, selectivity and stability.[2] Such research interest has inspired a number of gas sensors based on different sensing mechanisms, such as electrical, thermal, acoustic or optical properties.[3] Among these devices, the label-free sensors based on reflectometric interference[4,5] have proved to be an attractive and promising alternative for detecting chemical and gas vapors.[6–9] Generally, the interferometric gas sensor is dependent on the changes in the thin film refractive index due to the adsorption of the gases in the pores, and the shift of the optical thickness *nL* (product of refractive index and film thickness) in the reflected spectrum.[10] In order to achieve porous thin films that are usually preferred as interferometric sensor owing to their unique structure for gas adsorption,[11] tremendous efforts have been dedicated to the fabrication of a variety of porous structures including porous silicon, aluminum oxide (Al_2O_3) and titanium dioxide (TiO_2), which possess large surface area, and tunable surface chemistry.[12–14]

In addition, iron oxide (Fe_2O_3) with different kinds of structures is another platform for sensor application owning to its low cost, environmental friendliness and high stability.[15–18] However, the majority of the previously reported Fe_2O_3 based sensor are mainly based on their electrical properties and usually operate at high temperature. Moreover, complicated nanostructures (*e.g.*, urchin-like α-Fe_2O_3 nanostructures,[16] core–shell α-Fe_2O_3@SnO_2 hollow nanoparticles,[17] PbO loaded double-shell Fe_2O_3 hollow nanospheres[18]) are commonly needed, which are usually subject to tedious fabrication procedures with relatively high cost. Compared with conventional nanofabrication method, electrochemical anodization is a powerful method owing to its simplicity, reliability, high controllability and low cost.[19,20] Recently, anodic iron oxide nanostructures obtained by directly anodizing iron (Fe) metal have aroused wide interest in lithium-ion battery,[21,22] supercapacitor,[23] water splitting,[24] and fuel cell applications[25] because of its excellent optical, electrochemical and photocatalytic properties. However, to our knowledge, anodic α-Fe_2O_3 for optical sensing of volatile gas vapors have not been reported. Herein, we report a mesoporous α-Fe_2O_3 interferometer that was synthesized by anodization of Fe in ethylene glycol solution. Through varying the anodization condition, the mesoporous α-Fe_2O_3 nanostructures with well resolved Fabry–Perot fringes in the reflected spectrum were synthesized and further applied for detecting three organic vapors (hexane, acetone and isopropanol). The experiment results demonstrate that the α-Fe_2O_3 interferometer shows good sensitivity, reversibility and stability to the three organic vapors. Meanwhile, the α-Fe_2O_3 is also found to exhibit efficient photo-catalytic activity for the

---

[a] School of Materials Science and Engineering, Hefei University of Technology, Hefei, 230009, China. E-mail: ycwu@hfut.edu.cn

[b] School of Electronic Science and Applied Physics, Anhui Provincial Key Laboratory of Advanced Materials and Devices, Hefei University of Technology, Hefei, 230009, China. E-mail: jghu@hfut.edu.cn; luolb@hfut.edu.cn

degradation of the dodecane vapor residues in the α-Fe_2O_3 nanopores under visible light irradiation, therefore providing a self-cleaning platform for the future sensor application.

2. Experimental

2.1 Fabrication of porous α-Fe_2O_3 film

The mesoporous α-Fe_2O_3 structures were fabricated following a modified anodization process.[26] Firstly, the Fe foils (0.3 mm in thickness, 99.9% purity) were ultra-sonicated sequentially in acetone, ethanol and water. Then, the anodization was carried out in a two-electrode electrochemical cell, with the cleaned Fe foil and Pt as working anode and cathode, respectively (Fig. 1a). The Fe substrate was pressed together with an Al foil against an O-ring, defining a working area of 1.2 cm^2. The composition of the electrolyte was 0.1 mol L^{-1} NH_4F (96%, Aladdin) and 1 mol L^{-1} H_2O in an ethylene glycol (99%, Macklin) solution. Finally, the anodization experiment was carried out at 40 V for 30, 50, and 80 min respectively. To improve the crystallinity of Fe_2O_3, the as-fabricated specimen was further annealed in Ar atmosphere at 450 °C for 2 h prior to sensing test.

2.2 Sensor design and testing method

The setup for organic vapor sensing shown in Fig. 1b consists of a mesoporous α-Fe_2O_3 thin film mounted right below the transparent glass in a home-made Teflon flow cell. To measure the response of the sensor, the flow cell was assembled with an inlet connected to a glass bubbler. The statured organic vapors were firstly generated through purging air into the glass bubbler and then diluted to different concentrations by a certain amount of pure air. The flow-rate of the organic vapor was controlled by mass flow controllers. Tungsten light source focused through the microscope lens was put right above the flow cell and the reflection spectra of the sensor were collected through an Ocean Optics CCD spectrometer (USB 4000, Ocean optics, Inc.) from 400–1000 nm. By applying a fast Fourier transform (FFT) to the reflectance spectrum, the optical thickness of the film was calculated directly from the positions of the peaks in the FFT spectra. The FFT peaks were monitored in real-time to detect the optical thickness changes throughout the gas test. Note that the sensing experiment was all carried out at room temperature and the vapor concentrations were measured independently using a photoionization detector (ppbRAE, RAE Systems). Dodecane with a very low vapor pressure was used as a mode for the photocatalytic test. After the dosing and purging step, the contaminated optical sensor with dodecane was further irradiated by a 250 W metal halide lamp coupled with a UV cutoff filter ($\lambda > 420$ nm) (Xujiang Machine-Electronic Plant, Nanjing) for about 20 minutes. After irradiation, the optical thickness of the α-Fe_2O_3 was measured by the CCD spectrometer.

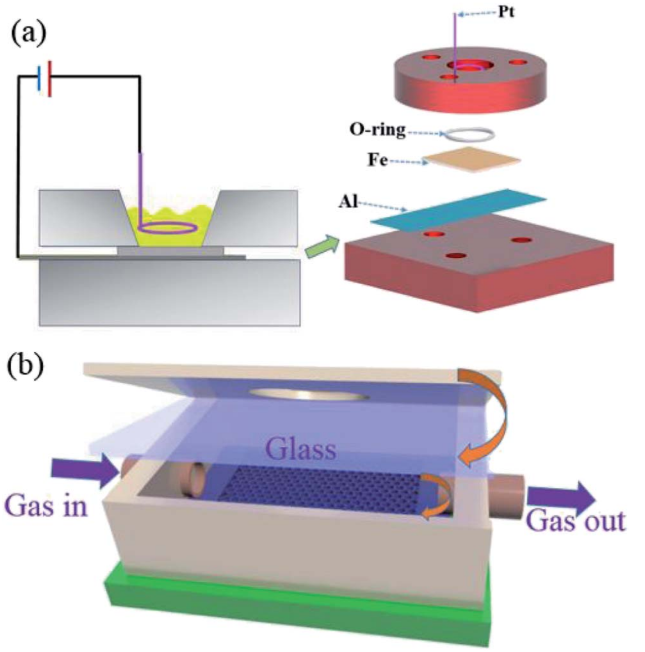

Fig. 1 (a) Schematic illustration of the setup for Fe foil anodization. (b) Schematic diagram of the flow-cell in the sensing experiment.

3. Results and discussion

The Fe anodization was performed under a positive potential which would form a mesoporous iron oxide layer over the Fe surfaces. Typically, the formation of anodic iron oxide in fluoride electrolytes is associated with the two competing processes: (1) the field assisted oxidation of iron to form iron oxide (eqn (1)); (2) the chemical dissolution of iron oxide by F^- in the solution (eqn (2)).[27,28] Usually, the formation of iron oxide continues to take place until an equilibrium is reached between the two competing reactions, following which the nanostructured iron oxide ceases development.

$$2Fe + 3H_2O \rightarrow Fe_2O_3 + 6H^+ \tag{1}$$

$$Fe^{3+} + 6F^- \rightarrow [FeF_6]^{3-} \tag{2}$$

Fig. 2a and b show the SEM images of the anodic Fe_2O_3 obtained at 30 min, displaying a porous structure with partially opened nanopores at the surface. With the anodic time increasing to 50 min, the top-view SEM images in Fig. 2c present fully open pores, while the cross-sectional SEM images exhibit vertically-oriented nanochannels from the top surface to the metal–oxide interfaces (Fig. 2d). The typical pore diameter is in the range of 30–50 nm, with an average value of 41 nm (Fig. 2h). When the anodization time was further increased to 80 min, the film thickness of the nanostructures keeps decreasing to about 4.5 μm and start to crumble due to the over-etching, as shown in Fig. 2e and f. Moreover, the pore diameter distribution of the as-obtained Fe_2O_3 is further investigated by top-view SEM analysis. It is observed that the diameters of the pores are in the range from 30 to 50 nm (Fig. 2g). It is noticed that compared with the anodization time at 30 min, the pore diameter anodized at 50 min increases from 23 nm to 41 nm. When the anodization time further increases to 60–80 min, the film thickness nearly keeps unchanged.

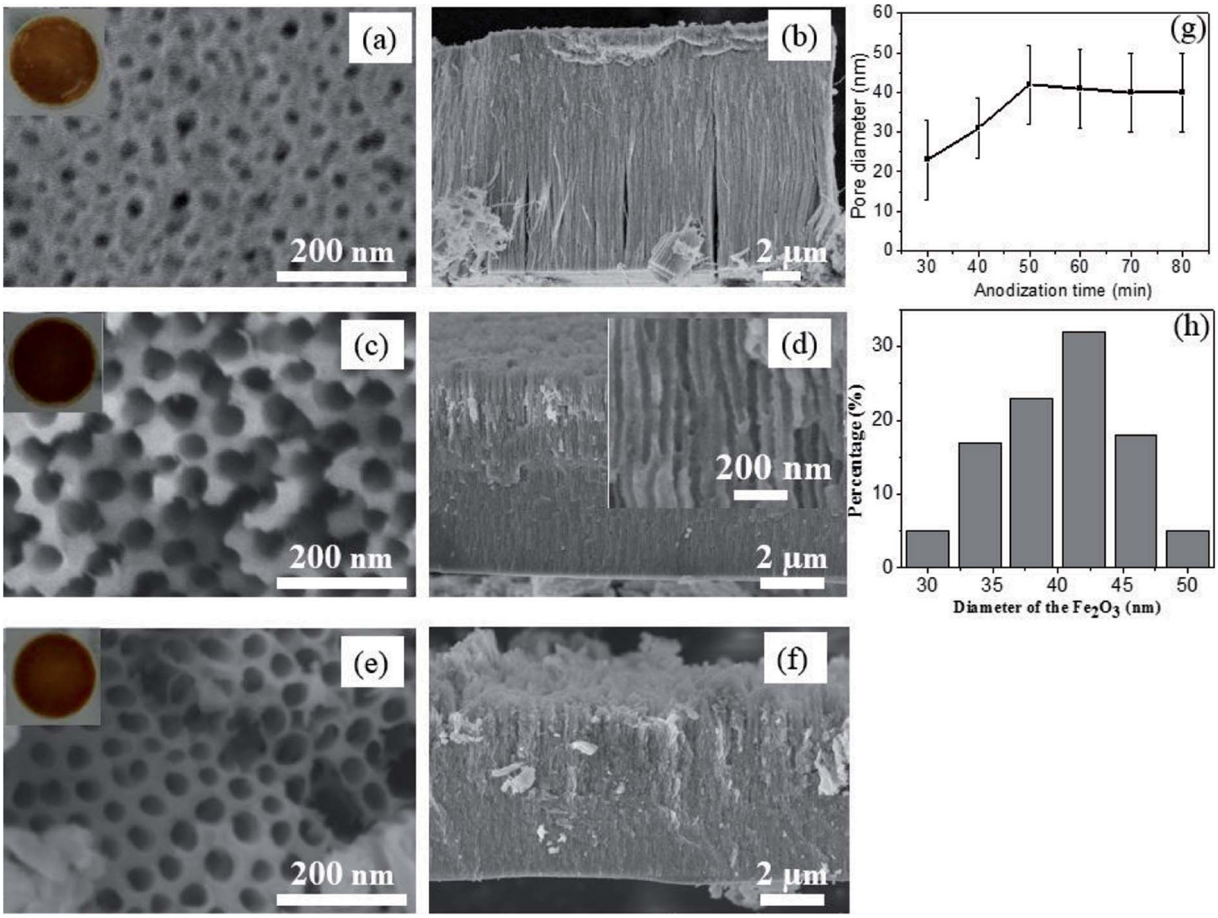

Fig. 2 The top view (a, c and e) and cross-sectional (b, d and f) SEM images of the anodic Fe_2O_3 under anodization time of 30, 50, and 80 minutes, respectively. (g) Pore diameter and length of the α-Fe_2O_3 anodized at different times. (h) The pore diameter distribution of the anodic α-Fe_2O_3 nanostructures with anodization time of 50 min.

Since the anodic Fe_2O_3 at low temperature is amorphous, the above as-anodized sample was further crystallized at 450 °C in argon atmosphere for 2 h. Fig. 3a shows the XRD patterns of the anodized sample before and after annealing. Clearly, the as-anodized Fe_2O_3 is amorphous with only a sharp Fe peak (dark line in Fig. 3a), but it will be converted into α-Fe_2O_3 (red line in Fig. 3a) after annealing at 450 °C. In addition, very small amount of Fe_3O_4 is observed, which may probably arise from the incomplete oxidation of the as-obtained α-Fe_2O_3 in the reducing atmosphere.[23,29] What is more, XPS analysis was carried out for further investigation of the oxidation states of the annealed Fe oxides in argon atmosphere. As shown in XPS survey spectrum (Fig. 3b), there exist three main peaks at around 284.8, 530.2, and 711.0 eV, which are assigned to be the characteristic peaks of C 1s, O 1s and Fe 2p, respectively. From further high resolution XPS spectrum of Fe 2p (Fig. 3c), two peaks at around 711.3 eV and 724.7 eV corresponding to the Fe 2p3/2 and Fe 2p1/2 spin orbit peaks of α-Fe_2O_3 are observed. Moreover, the Fe 2p2/3 and Fe 2p1/2 are accompanied by satellite structures on their high binding-energy sides, at around 719.9 eV and 732.9 eV respectively, which can be due to hematite (α-Fe_2O_3).[30] The high resolution spectrum of oxygen region displays two overlapping peaks with binding energies of 530.15 eV and 531.73 eV (Fig. 3d). The higher peak at 530.15 eV is attributed to the O 1s bound to Fe in the α-Fe_2O_3, while the lower one at 530.15 eV corresponds to the oxygen in the organic impurities exist in the sample surface. These XPS results demonstrate that the main composition of the annealed Fe oxide is α-Fe_2O_3, which is in accordance with the XRD results.

Next, the sensing mechanism of the mesoporous α-Fe_2O_3 is plotted in Fig. 4a, which is based on white light interference in the thin film. When light crosses an interface where the refractive index of the medium is different, a fraction of light is reflected and the left is transmitted. As shown in Fig. 4a, the incident light is reflected from the air/porous α-Fe_2O_3 and the porous α-Fe_2O_3/Fe substrate interfaces. As the two reflected waves overlap, they may interfere constructively and the Fabry–Perot fringes in a reflection spectrum are formed given that the extra path traversed by one wave is an integral number of wavelengths as described by the following equation:

$$m\lambda = 2nL \tag{3}$$

where m is an integer representing the spectral order, n is the mean refractive index of the porous layer and its contents, and L is the thickness of the porous layer. When the porous α-Fe_2O_3 interferometer is exposed to the organic vapor, the gas

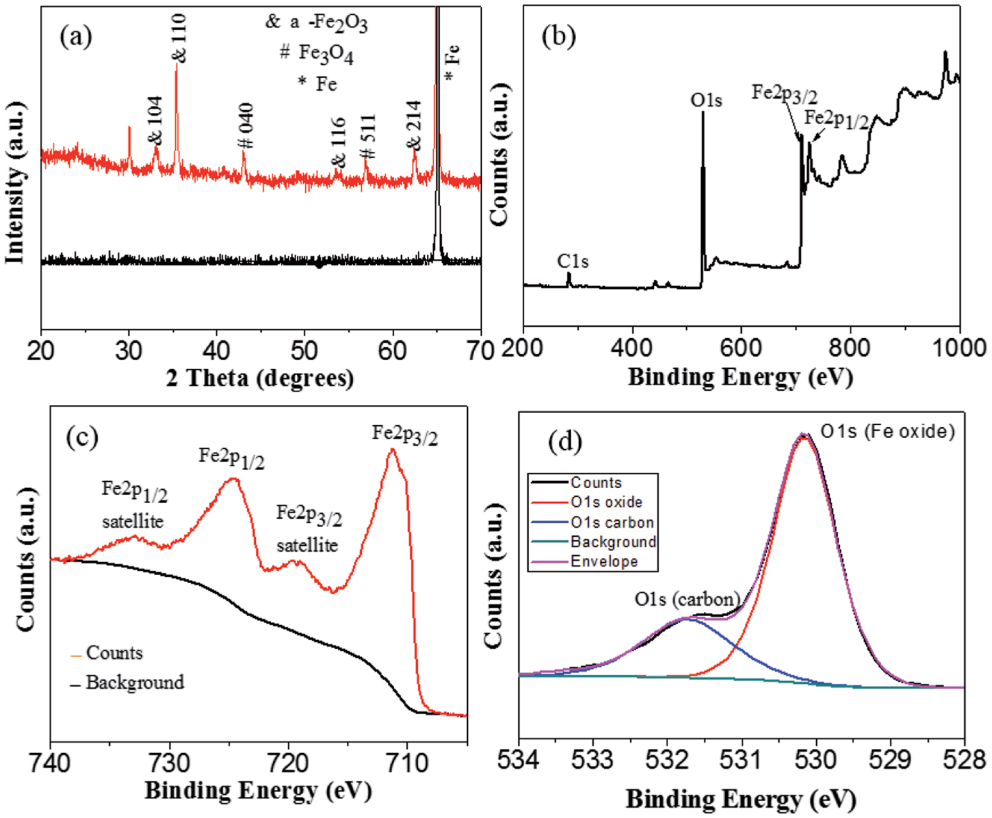

Fig. 3 (a) XRD patterns of the anodic Fe_2O_3 (anodization time: 50 min) before and after annealing in argon atmosphere. (b) XPS survey spectrum of the annealed anodic Fe_2O_3. XPS spectrum of Fe 2p (c) and O 1s (d) in high resolution.

molecular could adsorb or condensate into the pores of the mesoporous film promoted by the chemical reaction or capillary condensation effect.[11,14] Organic vapor in the pores is observed as a shift of the fringes to longer wavelengths, which is caused by the refractive indexes difference between the organic vapor and air. By applying a fast Fourier transform (FFT) to the

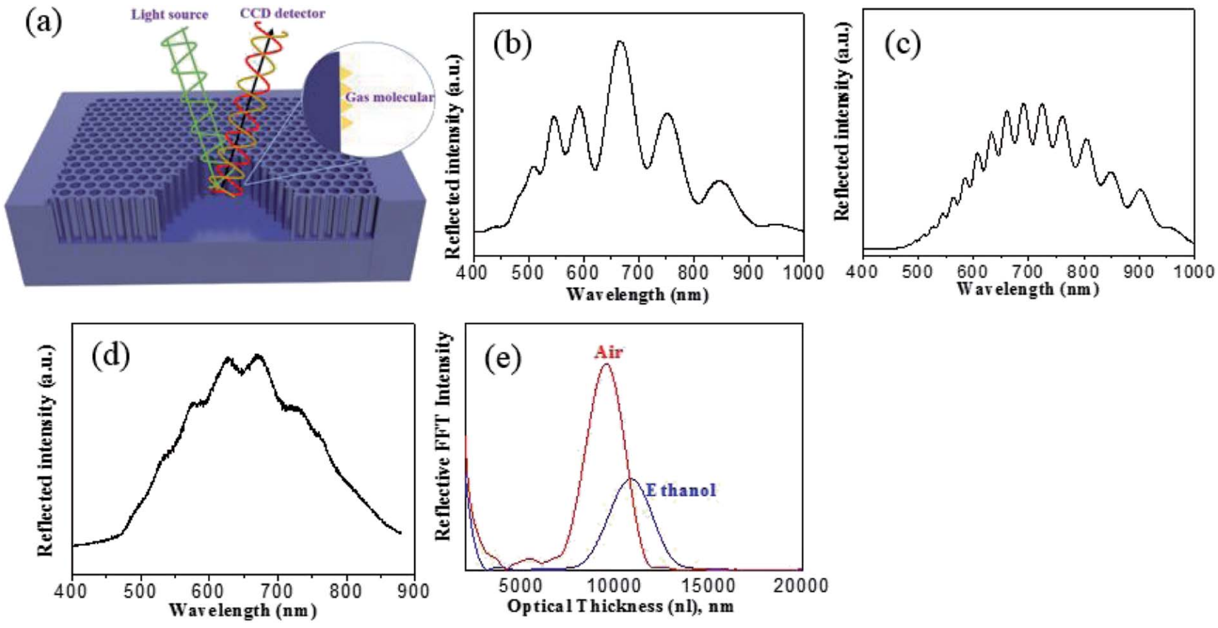

Fig. 4 (a) Schematic illustration of the α-Fe_2O_3 based interferometric vapor sensor. (b–d) Reflected spectrum of the α-Fe_2O_3 with anodization time of 30 min, 50 min and 80 min. (e) Reflective interferometric Fourier transform spectroscopy in air and ethanol of the α-Fe_2O_3 (anodization time: 50 min).

Table 1 Physical properties at room temperature (298 K)[33]

	Refractive index	Saturation vapor pressure (torr)
Acetone	1.359	233.3
Hexane	1.375	124
Isopropanol	1.377	45
Dodecane	1.422	0.134

as-obtained reflective spectrum which is referred as reflective interferometric fourier transform spectroscopy (RIFTS),[31,32] the detection of the vapor is achieved through the analysis of the optical thickness (*nL*) calculated by the RIFTS.

The reflectance spectra were measured at normal incidence using a bifurcated optic fiber, with one end connected to a tungsten lamp while the other to a CCD spectrometer as previously reported.[14] The tungsten light source was focused by a microscope objective lens onto the surface of the film and the corresponding reflected light from the film was collected by the same microscope and recorded by the CCD detector. Fig. 4b–d compares the reflection spectra with Fabry–Perot fringes obtained from anodic α-Fe_2O_3 with different anodization time. It is seen that the mesoporous α-Fe_2O_3 with smooth and fully opened pores anodized at 50 min (Fig. 4c) displays the best interference fringes in comparison with other two samples obtained at 30 min (partially opened pores) and 80 min (partially destroyed structure). In light of this, the anodic α-Fe_2O_3 from 50 min anodization are chosen for the following sensing measurement. Through immersing the α-Fe_2O_3 thin film into ethanol, the optical thickness and porosity could be determined by the spectroscopic liquid infiltration method (SLIM).[32] In this method, the reflection spectrum of α-Fe_2O_3 was collected in both air and ethanol at the same spot. By applying FFT to the reflectance spectrum, the FFT intensity *versus* optical thickness could be obtained in Fig. 4e, from which an apparent red shift of optical thickness is observed upon submerging the film in ethanol. The change of optical thickness arises from the difference between the reflective indexes of air ($n = 1$) and ethanol ($n = 1.3611$), and is highly dependent on the porosity and film thickness of the materials. Therefore through a least-squares fit of the two optical thicknesses (in air and ethanol) to a two component Bruggeman effective medium approximation, the porosity and film thickness of α-Fe_2O_3 interferometer are finally obtained to be 38.3 ± 1.8% and 6230 ± 56 nm, respectively, which agree reasonably well with the value measured from SEM study.

In order to evaluate the sensing ability of the mesoporous α-Fe_2O_3 interferometers for volatile organic vapors, three organics (hexane, acetone, and isopropanol (IPA)) with different refractive index and vapor pressure (Table 1) were tested.[33] It is worth noting that even though the three organic vapors have nearly close reflective index, yet, their vapor pressures are completely different, which also plays an important role in determining the sensitivity. During the vapor sensing process, due to the capillary condensation effect,[11] gas vapor with a lower vapor pressure

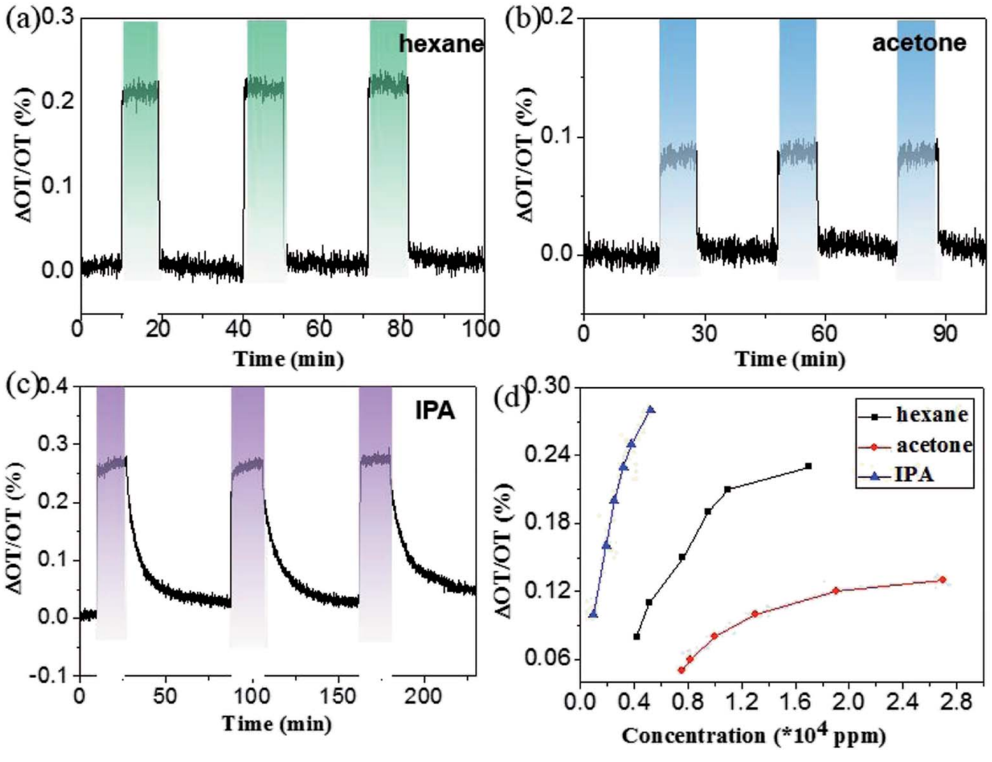

Fig. 5 Dose–response curves of the Fe_2O_3 interferometer to hexane (a), acetone (b) and isopropanol (c) respectively. (d) Response curves for hexane, acetone and IPA at different concentrations. The quantity ΔOT/OT (%) is equal to $(nL_{\text{final}} - nL_{\text{initial}})/nL_{\text{initial}} \times 100\%$, nL_{final} and nL_{initial} represent the optical thickness at time 0 and *T*, respectively.

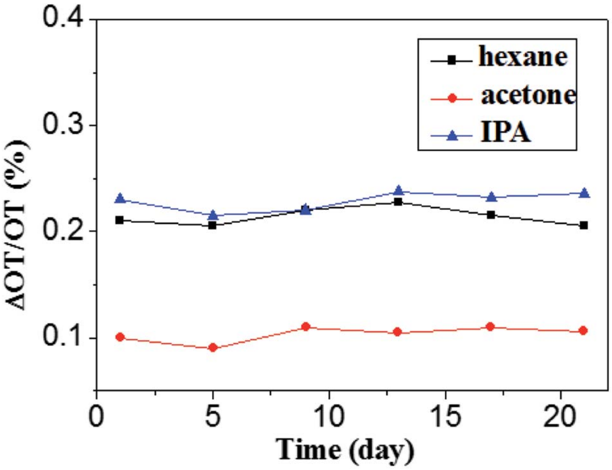

Fig. 6 Long-term stability of the Fe_2O_3 interferometer to hexane (11 000 ppm), acetone (13 000 ppm) and isopropanol (2000 ppm) respectively.

will induce more condensed vapors in the inner pores[14] and should translate to larger changes in optical thickness (nL) upon exposure to the analytes.

Fig. 5a–c shows the dose–response curves for hexane, acetone and IPA, respectively, from which one can readily find that our device displays different sensitivity to the three gases. As expected, it has the most sensitive response to IPA with the lowest vapor pressure, only 2800 ppmv will generate about 0.25% change in optical thickness. For hexane, 11 000 ppmv is able to induce about 0.2% change in optical thickness. The acetone is the most insensitive, a concentration of 13 000 ppmv only results in about 0.1% change in optical thickness. Further observation of the curves after the dosing found that the signal dropped quickly to the original baseline for hexane and acetone, while a purging time of about 1 h was needed for IPA to return to its original baseline level. The difficulty for desorption of IPA in the mesoporous film is probably related to either the lowest vapor pressure or the hydrophilic properties of Fe_2O_3 and IPA that may cause the formation of hydrogen bonds between them.[14] Fig. 5d plots the relationship between optical thickness change and concentrations for three organic vapors. Obviously, to generate the same ΔOT/OT, acetone needs the largest concentration, while IPA the least. To evaluate the detection limit of the α-Fe_2O_3 based interferometer, an S/N ratio of 2 was used. The detection limits of the present porous Fe_2O_3 interferometer for hexane, acetone and IPA were determined to be 1100, 3600 and 65 ppmv, respectively. The sensitivity for IPA is comparable to other well-established interferometer-based optical sensors, *e.g.*, porous silicon and anodic TiO_2.[14,34] The long-term stability of the α-Fe_2O_3 based interferometer was also measured and shown in Fig. 6. It can be easily seen that the sensor exhibits good stability even the sample was stored in ambient condition for 3 weeks.

As often in other gas sensors, the present α-Fe_2O_3 interferometer also suffer from contamination due to gas adsorption after repeated sensing, which constitutes main bottleneck for further application.[34,35] Fig. 7a shows the dose–response curve to dodecane with a low vapor pressure of 0.134 torr. A remarkable increase in optical thickness was immediately observed after dodecane vapor introduced into the nonporous Fe_2O_3 chamber. However, due to the strong tendency of condensation, it is difficult to remove the dodecane even by extended air purging. Considering the fact that the α-Fe_2O_3 is a typical semiconductor with a bandgap of 2.0 eV and it has proved to be a good photo-catalyst for RhB and other organic chemicals degradation under visible light illumination,[36,37] we tried to refresh the sensing ability by shining the porous α-Fe_2O_3 interferometer with visible light. Fig. 7b depicts the optical thickness shift of 20 cycles filling and visible light cleaning. Notably, when the above contaminated sample after air purging were further illuminated under a 250 W metal halide lamp (with the UV cutoff) for about 20 minutes, the optical thickness was substantially decreased and virtually recovered to its original value. This means our optical sensor is almost recovered to its original state after visible light refreshment, demonstrating good self-cleaning reversibility and repeatability of the α-Fe_2O_3 based interferometer. The self-cleaning mechanism of the α-

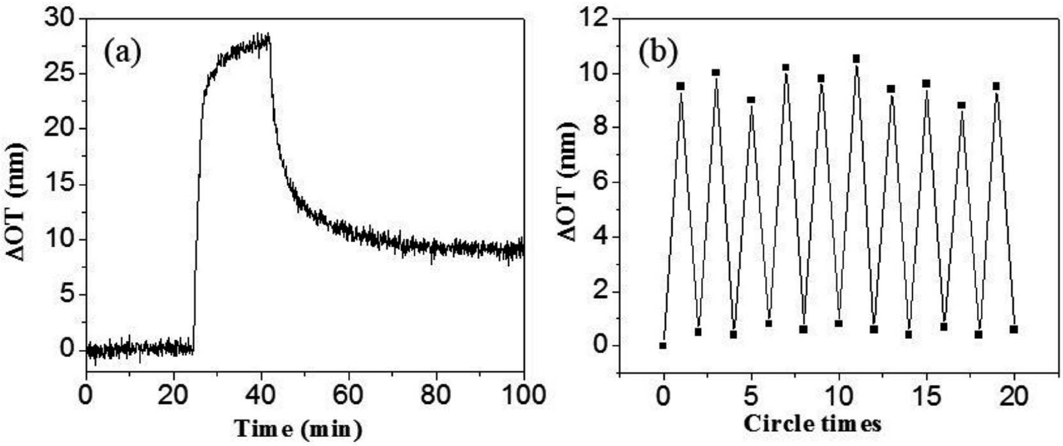

Fig. 7 (a) Dose–response curves of the Fe_2O_3 interferometer to dodecane. (b) Optical thickness changes during the 10 cycles filling and cleaning. The quantity ΔOT is equal to $nL_{\text{final}} - nL_{\text{initial}}$, nL_{final} and nL_{initial} represent the optical thickness at time 0 and T, respectively in (a). In (b), ΔOT represents two states: nL changes after dodecane dosing and air purging, nL changes after visible light cleaning.

Fe_2O_3 interferometer in the air can be explained as follows: as α-Fe_2O_3 is irradiated by visible light, holes and electron pairs are created and electron could react with O_2 to generate highly reactive superoxide anion radicals ($\cdot O_2$), (eqn (4) and (5)). The $\cdot O_2$ are extremely reactive and are able to decompose the organic vapors in the pores of the α-Fe_2O_3 interferometer.[33]

$$\alpha\text{-}Fe_2O_3 + h\nu \rightarrow e^- + h^+ \quad (4)$$

$$e^- + O_2 \rightarrow \cdot O_2^- \quad (5)$$

4. Conclusions

In summary, mesoporous α-Fe_2O_3 interferometers with well-resolved optical fringes were fabricated by an anodization method. The as-fabricated α-Fe_2O_3 interferometers were applied as optical sensor for various gases detection. The response of the α-Fe_2O_3 interferometer to different analyte was found to strongly depend on the physical properties of the analyte. The lower the vapor pressure of the analyte, the better the sensitivity will be. Moreover, we have also investigated the self-cleaning ability of the fabricated α-Fe_2O_3 sensor. With the aid of visible light illumination, the gas sensor was able to recover effectively with good reproducibility and reversibility. These results suggests that the as-fabricated mesoporous α-Fe_2O_3 interferometer is an attractive sensing material for effective detection of organic vapors with good self-recovery ability.

Conflicts of interest

There are no conflicts to declare.

Acknowledgements

This work was supported by the National Natural Science Foundation of China (NSFC, No. 21501038, 61575059, 61675062), the Fundamental Research Funds for the Central Universities (2014HGCH0005).

References

1 E. Comini, Metal oxide nano-crystals for gas sensing, *Anal. Chim. Acta*, 2006, **568**, 28–40.

2 V. K. Khanna, *Nanosensors physical, chemical, and biological*, 1st edn, CRC Press, 2012.

3 A. Mirzaei, S. G. Leonardi and G. Neri, Detection of hazardous volatile organic compounds (VOCs) by metal oxide nanostructures-based gas sensors: A review, *Ceram. Int.*, 2016, **42**, 15119–15141.

4 C. Pacholski, C. Yu, G. M. Miskelly, D. Godin and M. J. Sailor, Reflective interferometric fourier transform spectroscopy: A self-compensating label-free immunosensor using double-layers of porous SiO_2, *J. Am. Chem. Soc.*, 2006, **128**, 4250–4252.

5 A. Brecht, G. Gauglitz and W. Nahm, Interferometric measurements used in chemical and biochemical sensors, *Analysis*, 1990, **20**, 135–140.

6 B. P. Mohrle, K. Kohler, J. Jaehrling, R. Brock and G. Gauglitz, Label-free characterization of cell adhesion using reflectometric interference spectroscopy (RIfS), *Anal. Bioanal. Chem.*, 2006, **384**, 407–413.

7 G. Gauglitz, A. Brecht, G. Kraus and W. Mahm, Chemical and biochemical sensors based on interferometry at thin (multi) layers, *Sens. Actuators, B*, 1993, **11**, 21–27.

8 A. Santos, T. Kumeria and D. Losic, Nanoporous anodic aluminum oxide for chemical sensing and biosensors, *TrAC, Trends Anal. Chem.*, 2013, **44**, 25–38.

9 A. Santos, V. S. Balderrama, M. Alba, P. Formentin, J. Ferre-Borrull, J. Pallares and L. F. Marsal, Nanoporous anodic alumina barcodes: toward smart optical biosensors, *Adv. Mater.*, 2012, **24**, 1050–1054.

10 M. J. Sailor, *Porous silicon in practice: preparation, characterization, and applications*, Wiley-VCH, Wenham, Germany, 2012.

11 F. Casanova, C. E. Chiang, C. P. Li, I. V. Roshchin, A. M. Ruminski, M. J. Sailor and I. K. Schuller, Gas adsorption and capillary condensation in nanoporous alumina films, *Nanotechnology*, 2008, **19**, 315709.

12 F. X. Liang, J. Z. Wang, Y. Wang, Y. Lin, L. Liang, Y. Gao and L. B. Luo, Single-layer graphene/titanium oxide cubic nanorods array/FTO heterojunction for sensitive ultraviolet light detection, *Appl. Surf. Sci.*, 2017, **426**, 391–398.

13 T. Kumeria and D. Losic, Controlling interferometric properties of nanoporous anodic aluminium oxide, *Nanoscale Res. Lett.*, 2012, **7**, 88.

14 F. X. Liang, T. L. Kelly, L. B. Luo, H. Li, M. J. Sailor and Y. Y. Li, Self-cleaning organic vapor sensor based on a nanoporous TiO_2 interferometer, *ACS Appl. Mater. Interfaces*, 2012, **4**, 4177–4183.

15 J. J. Ouyang, J. Pei, Q. Kuang, Z. X. Xie and L. S. Zheng, Supersaturation-controlled shape evolution of alpha-Fe_2O_3 nanocrystals and their facet-dependent catalytic and sensing properties, *ACS Appl. Mater. Interfaces*, 2014, **6**, 12505–12514.

16 P. Sun, W. Wang, Y. P. Liu, Y. F. Sun, J. Ma and G. Y. Lu, Hydrothermal synthesis of 3D urchin-like α-Fe_2O_3 nanostructure for gas sensor, *Sens. Actuators, B*, 2012, **173**, 52–57.

17 Q. X. Yu, J. H. Zhu, Z. Y. Xu and X. T. Huang, Facile synthesis of α-Fe_2O_3@SnO_2 core-shell heterostructure nanotubes for high performance gas sensors, *Sens. Actuators, B*, 2015, **213**, 27–34.

18 P. Sun, B. Q. Wang, L. P. Zhao, H. Y. Gao, T. S. Wang, X. L. Yang, C. Liu and G. Y. Lu, Enhanced gas sensing by amorphous double-shell Fe_2O_3 hollow nanospheres functionalized with PdO nanoparticles, *Sens. Actuators, B*, 2017, **252**, 322–329.

19 J. M. Macak, M. Zlamal, J. Krysa and P. Schmuki, Self-organized TiO_2 nanotube layers as highly efficient photocatalysts, *Small*, 2007, **3**, 300–304.

20 A. Ghicov and P. Schmuki, Self-ordering electrochemistry: a review on growth and functionality of TiO_2 nanotubes and other self-aligned MO_x structures, *Chem. Commun.*, 2009, **40**, 2791–2808.

21 K. Y. Xie, Z. G. Lu, H. T. Huang, W. Lu, Y. Q. Lai, J. Li, L. M. Zhou and Y. X. Liu, Iron supported C@Fe_3O_4 nanotube array: a new type of 3D anode with low-cost for high performance lithium-ion batteries, *J. Mater. Chem.*, 2012, **22**, 5560–5567.

22 H. Cheng, Z. G. Lu, R. G. Ma, Y. C. Dong, H. E. Wang, L. J. Xi, L. X. Zheng, C. K. Tsang, H. Li, C. Y. Chung, J. A. Zapien and Y. Y. Li, Rugated porous Fe_3O_4 thin films as stable binder-free anode materials for lithium ion batteries, *J. Mater. Chem.*, 2012, **22**, 22692–22698.

23 K. Y. Xie, J. Li, Y. Q. Lai, W. Lu, Z. A. Zhang, Y. X. Liu, L. M. Zhou and H. T. Huang, Highly ordered iron oxide nanotube arrays as electrodes for electrochemical energy storage, *Electrochem. Commun.*, 2011, **13**, 657–660.

24 B. Lucas-Granados, R. Sánchez-Tovar, R. M. Fernández-Domene and J. García-Antón, Study of the annealing conditions and photoelectrochemical characterization of a new iron oxide bi-layered nanostructure for water splitting, *Sol. Energy Mater. Sol. Cells*, 2016, **153**, 68–77.

25 Y. D. Xue, W. Jin, H. Du, S. N. Wang, S. L. Zheng and Y. Zhang, Tuning a-Fe_2O_3 nanotube arrays for the oxygen reduction reaction in alkaline media, *RSC Adv.*, 2016, **6**, 41878–41884.

26 T. J. LaTempa, X. J. Feng, M. Paulose and C. A. Grimes, Temperature-Dependent Growth of Self-Assembled Hematite (alpha-Fe_2O_3) Nanotube Arrays: Rapid Electrochemical Synthesis and Photoelectrochemical Properties, *J. Phys. Chem. C*, 2009, **113**, 16293–16298.

27 D. Kowalski, D. Kim and P. Schmuki, TiO_2 nanotubes, nanochannels and mesosponge: Self-organized formation and applications, *Nano Today*, 2013, **8**, 235–265.

28 T. J. LaTempa, X. J. Feng, M. Paulose and C. A. Grimes, Temperature-dependent growth of self-assembled hematite (α-Fe_2O_3) nanotube Arrays : Rapid Electrochemical Synthesis and Photoelectrochemical Properties, *J. Phys. Chem. C*, 2009, **113**, 16293–16298.

29 B. Sarma, A. L. Jurovitzki, Y. R. Smith, R. S. Ray and M. Misra, Influence of annealing temperature on the morphology and the supercapacitance behavior of iron oxide nanotube (Fe-NT), *J. Power Sources*, 2014, **272**, 766–775.

30 A. A. Tahir, K. G. U. Wijayantha, S. Saremiyarahmadi, M. Mazhar and V. Mckee, Nanostructured α-Fe_2O_3 thin films for photoelectrochemical hydrogen generation, *Chem. Mater.*, 2009, **21**, 3763–3772.

31 C. Pacholski, C. Yu, G. M. Miskelly, D. Godin and M. J. Sailor, Reflective interferometric fourier transform spectroscopy: a self-compensating label-free immunosensor using double-layers of porous SiO2, *J. Am. Chem. Soc.*, 2006, **128**, 4250–4252.

32 C. Pacholski, M. Sartor, M. J. Sailor, F. Cunin and G. M. Miskelly, Biosensing using porous silicon double-layer interferometers: reflective interferometric fourier transform spectroscopy, *J. Am. Chem. Soc.*, 2005, **127**, 11636–11645.

33 *CRC Handbook of Chemistry and Physics*, 60th edn, CRC Press, Inc., Boca Raton, FL, 1980.

34 T. L. Kelly, T. Gao and M. J. Sailor, Carbon nanofiber photonic crystals: carbon and carbon/silicon composites templated in rugate filters for the adsorption and detection of organic vapors, *Adv. Mater.*, 2011, **23**, 1776–1781.

35 Y. Y. Song, F. Schmidt-Stein, S. Berger and P. Schmuki, TiO_2 nano test tubes as a self-cleaning platform for high-sensitivity immunoassays, *Small*, 2010, **6**, 1180–1184.

36 Z. H. Zhang, M. Faruk Hossain and T. Takahashi, Fabrication of shape-controlled α-Fe_2O_3 nanostructures by sonoelectrochemical anodization for visible light photocatalytic application, *Mater. Lett.*, 2010, **64**, 435–438.

37 R. Chen, J. Lu, J. Xiao, C. Z. Zhu, S. C. Peng and T. H. Chen, α-Fe_2O_3 supported Bi_2WO_6 for photocatalytic degradation of gaseous benzene, *Solid State Sci.*, 2017, **71**, 14–21.